Halide segregation governs interfacial charge-transfer pathways in mixed-halide perovskites

Jae Eun Lee,[a] Robert D. J. Oliver, [b] Joshua R. S. Lilly,[a] Rehmat Sood-Goodwin, [cd] Aleksander M. Ulatowski,[a] Alexandra J. Ramadan, [c] Henry J. Snaith, [a] Michael B. Johnston [a] and Laura M. Herz [*a]

Mixed-halide perovskites offer ideal bandgaps for tandem solar cells, but they suffer from light-induced halide segregation, which compromises their operational stability. Here, we directly probe the impact of halide segregation on charge-carrier dynamics at the interface between a mixed-halide perovskite and charge transport layers by using a free-space synchronous multimodal spectroscopy approach, combining time-resolved microwave conductivity, time-resolved photoluminescence (PL) and steady-state PL. We present a method to distinguish directly between charge-carrier dynamics dominated by either majority or minority carriers, enabling us to isolate effects arising from charge-selective extraction from the perovskite to commonly used hole- or electron transport layers, i.e. poly[bis(4-phenyl)(2,4,6-trimethylphenyl)amine] (PTAA) and SnO_2, respectively. We show that halide segregation creates iodide-rich phases that capture charge carriers within sub-nanoseconds, which slightly reduces their mobilities at microwave frequencies. We reveal that charge extraction from such iodide-rich domains is still surprisingly feasible, but competes with enhanced radiative recombination resulting from higher charge concentrations caused by funnelling into these minority phases. We demonstrate that together such effects reduce charge diffusion lengths and can account for the widely observed reduction in open-circuit voltages and short-circuit currents in solar cells under operational conditions. Our findings unravel the causes underpinning the adverse impact of halide segregation and provide guidelines to improve device performance.

Broader context

Photovoltaics play a critical role in the global transition to renewable energy, with installed capacity now exceeding 2 terawatts. Continued momentum will depend on further breakthroughs in efficiency and stability which multijunction architectures such as perovskite/silicon tandem solar cells may deliver. In this context, wide-bandgap mixed-halide perovskites have emerged as ideal top-cell absorbers because their bandgaps can be readily tuned to complement underlying subcells. However, their operational stability is limited by light-induced halide segregation during which the initially homogenous mixed-phase perovskite separates into iodide-rich and bromide-rich domains. Understanding and quantifying such effects in multilayer architectures remains a substantial challenge. Here, we demonstrate a novel synchronous multimodal spectroscopy to unveil the complex interplay between halide segregation, charge transport and recombination. We show that in perovskite heterojunctions formed with charge-transport layers, charge extraction remains feasible from iodide-rich domains formed through halide segregation. However, such domains experience reduced diffusion lengths because charge mobility is reduced and extraction competes against enhanced radiative recombination resulting from charge funneling into iodide-rich domains. Both short-circuit currents and open-circuit voltages may therefore be lowered through halide segregation. These insights reveal the microscopic consequences of halide segregation and provide guidance for mitigating its impact in next-generation tandem solar cells.

*a*Department of Physics, University of Oxford, Clarendon Laboratory, Parks Road, Oxford, OX1 3PU, UK. E-mail: laura.herz@physics.ox.ac.uk

*b*School of Chemical, Materials and Biological Engineering, University of Sheffield, Sir Robert Hadfield Building, Mappin Street, Sheffield, S1 3JD, UK

*c*School of Mathematical and Physical Sciences, University of Sheffield, Hicks Building, Hounsfield Road, Sheffield, S3 7RH, UK

*d*Grantham Centre for Sustainable Futures, University of Sheffield, Sheffield, S10 2TN, UK

Introduction

Recent advances in photovoltaics research have been strongly driven by the remarkable rise in the performance of metal halide perovskite/silicon tandem solar cells, which have now achieved a record power conversion efficiency (PCE) in excess of 34%,[1,2] surpassing the detailed balance limit of single-junction solar cells. In general, two-terminal tandem solar cells require a combination of a wide bandgap semiconductor (>1.7 eV) and a narrow bandgap semiconductor (<1.4 eV) to reduce

thermalisation losses while maintaining the current-matching condition.[3–5] Lead iodide-bromide perovskites are typically employed as the wide bandgap absorber because their bandgaps can be readily tuned by varying the iodide-bromide ratio,[6,7] offering tailored wide bandgaps to complement the bandgap of the narrow bandgap subcell to achieve an optimal tandem PCE.

However, such mixed-halide perovskites typically suffer from halide segregation where prolonged exposure to light or electric bias drives the spatial separation of the mixed-phase perovskite into both an iodide-rich (I-rich) and a bromide-rich phase.[8–10] Various models have been proposed to explain the mechanism of halide segregation, ranging from thermodynamic driving forces to polaronic and defect-mediated models.[9,11–18] However, a comprehensive theory explaining the underlying mechanism of halide segregation remains elusive, owing to the complex interplay of ionic movement with external perturbations as well as morphology, strain, crystallinity and composition of the perovskite thin film.[10,19–26] Nevertheless, halide segregation is known to adversely affect the optoelectronic properties of metal halide perovskites for tandem applications: the formation of I-rich domains of lower band gap induces photoexcited charge carriers to funnel into these domains, effectively red-shifting the targeted wide bandgap, and ultimately compromising the overall device performance by reducing both open-circuit voltage (V_{OC}) and short-circuit current (J_{SC}).[25,27–30] Motti et al. have revealed that in lead mixed-halide perovskite films, such charge-carrier funnelling occurs on the timescale of tens of picoseconds, enhancing the effective radiative recombination owing to the increased charge-carrier density in the I-rich domains.[31] However, mitigating device performance losses following halide segregation urgently requires a comprehensive understanding of charge-carrier dynamics associated with the interface between mixed-halide perovskites and charge transport layers. In such half-stack architectures, a range of additional processes occur, including charge transfer across and non-radiative recombination at the heterojunction interface, which are known to be critical to the performance of wide-bandgap mixed-halide perovskite photovoltaics.[27,32–34] Such processes in turn may be affected by halide segregation in a variety of ways, which remain largely unexplored.

Here, we reveal how halide segregation moderates the charge-carrier dynamics associated with the interface of the prototypical wide bandgap perovskite $FA_{0.83}Cs_{0.17}Pb(I_{0.6}Br_{0.4})_3$ with commonly used charge transport layers, either the hole transport layer (HTL) poly[bis(4-phenyl)(2,4,6-trimethylphenyl) amine] (PTAA) or the electron transport layer (ETL) SnO_2. We utilise a synchronous multimodal spectroscopy approach, combining time-resolved microwave photoconductivity (TRMC), time-resolved photoluminescence (TRPL), and steady-state photoluminescence (ssPL) to monitor and evaluate the impact of halide segregation. This multimodal approach allows us to disentangle contributions arising from either intrinsic radiative electron–hole recombination or charge-selective extraction by PTAA or SnO_2 layers. We show that halide segregation leads to funnelling of charge carriers into I-rich domains on a sub-nanosecond timescale where they experience a slight reduction in mobility at microwave frequencies. We further

demonstrate that charge-carrier extraction subsequently occurs through the I-rich phase, and that it is still remarkably effective. However, such extraction competes with enhanced radiative recombination driven by the enhanced charge-carrier density in these domains, which, in conjunction with a reduction in mobility, limits charge-carrier diffusion lengths and thereby extraction. We further evaluate the impact of such effects on predicted solar cell performance parameters.

Results and discussion

Synchronous multimodal time-resolved conductivity and photoluminescence approach

To address the complex charge-carrier dynamics arising from halide segregation, we employ a synchronous multimodal spectroscopy approach illustrated in Fig. 1a. We simultaneously record TRMC, TRPL and ssPL for the same thin-film location under identical excitation conditions, enabling us to probe charge-carrier funnelling as well as the competition between enhanced radiative loss and charge-carrier extraction originating from halide segregation. To investigate the impact of halide segregation on such dynamics, films were exposed to 532 nm continuous wave (CW) illumination at a power density of 150 mW cm^{-2} for the duration of 6 hours (see Fig. 1a). Such long CW illumination was required to drive significant halide segregation, given that $FA_{0.83}Cs_{0.17}Pb(I_{0.6}Br_{0.4})_3$ is a relatively phase stable material undergoing minimal halide segregation even after prolonged pulsed excitation (see Fig. S1).[9,31] We note that the instantaneous charge-carrier density generated by such long-term background CW illumination is orders of magnitude lower than that injected by the 530 nm pulsed excitation we employed to record TRPL and TRMC and therefore does not significantly affect the analysis of the recombination dynamics.[31] Moreover, the photon energies for the pulsed excitation and CW illumination lie below the bandgaps of the PTAA and SnO_2 transport layers, thereby preventing parasitic absorption and ensuring selective excitation of only the perovskite.[35,36]

To enable the multimodal approach, the TRMC signal is recorded in a free-space transmission geometry, and based on a high-frequency (102 GHz) microwave probe[37] to solely detect photoconductivity arising from free charge carriers and limit any contributions from slow ionic motion.[38] To simultaneously probe PL dynamics arising from either the mixed phase or the I-rich phase, TRPL is detected by two fast photodiodes across two separate spectral windows, selected with bandpass (BP) filters at 658–694 nm and 800–850 nm, respectively. These windows capture the higher-energy tail of the mixed-phase PL and the lower-energy tail of the I-rich phase PL, providing sufficient spectral separation for the two signals not to overlap. A fibre-coupled ssPL probe monitors time-integrated emission spectra as a proxy for the extent and evolution of halide segregation. Further details of the experiment can be found in the Methods section below.

We chose the multimodal TRMC and TRPL approach because it allows for direct distinction between charge-carrier dynamics dominated by either majority or minority carriers.
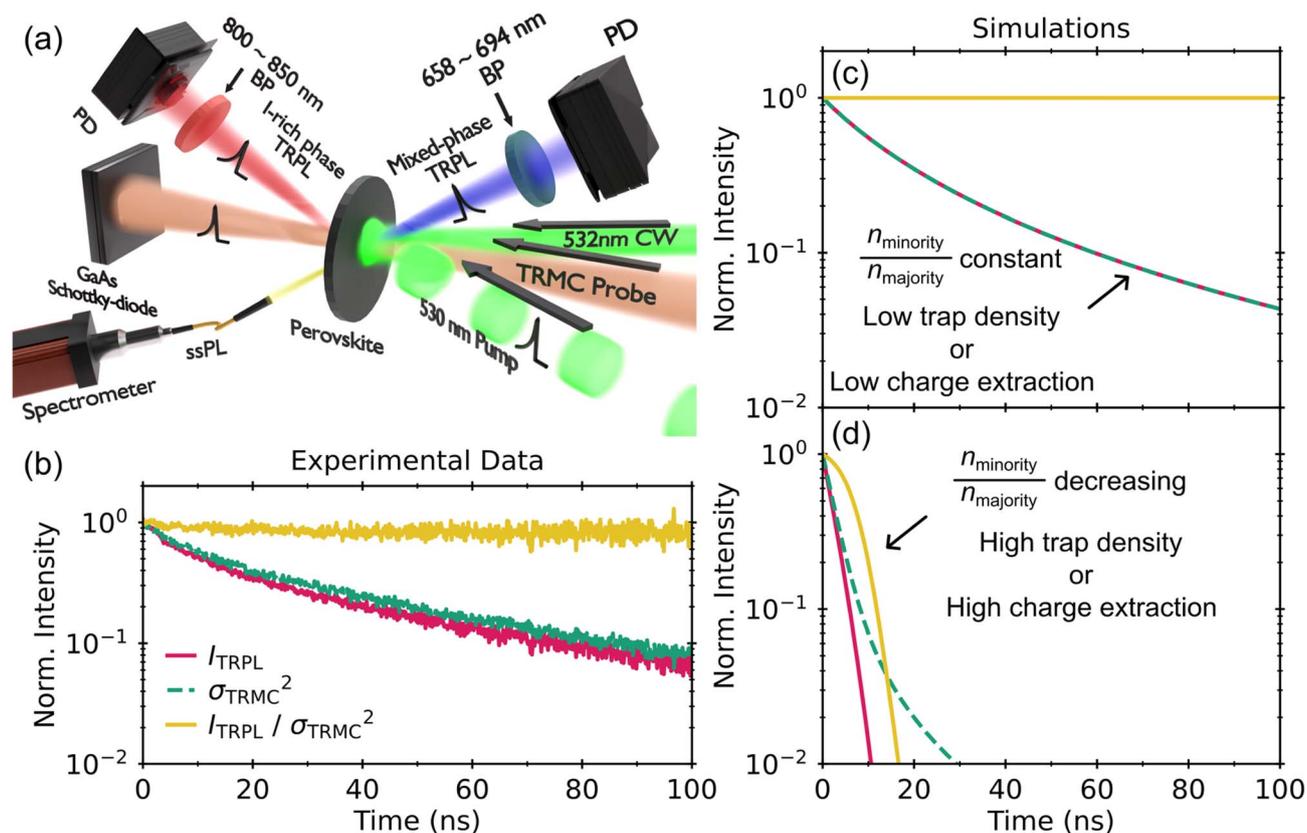
Fig. 1 (a) Synchronous multimodal spectroscopy system, enabling simultaneous acquisition of time-resolved photoluminescence (TRPL), time-resolved microwave conductivity (TRMC), and steady-state photoluminescence (ssPL). TRPL is filtered into two spectral windows, one to isolate the mixed phase (658–694 nm bandpass (BP) filter) and another the I-rich phase (800–850 nm BP filter), and detected with fast photodiode detectors (PD). TRMC is detected with a GaAs Schottky diode in transmission geometry. ssPL is detected with a fibre-coupled spectrometer. (b) Representative transients measured for a Quartz/FA$_{0.83}$Cs$_{0.17}$Pb(I$_{0.6}$Br$_{0.4}$)$_3$/PMMA thin-film stack photoexcited with a 530 nm pulsed laser at a fluence of 3.6 μJ cm^{-2}. I_{TRPL} denotes the TRPL intensity transient with 658–694 nm BP filter, σ_{TRMC}^2 the square of the TRMC transient and I_{TRPL}/σ_{TRMC}^2 the ratio between I_{TRPL} and σ_{TRMC}^2. (c) Simulated transients for the case of low trap density or low charge extraction, and (d) Simulated transients for the case of high trap density or high charge extraction (full details of simulations provided in SI Note 2). Panels (b), (c) and (d) share the same legend.

Through judicious analysis, these combined non-contact probes[37,39] can reveal whether charge-carrier dynamics are dominated by intrinsic radiative electron–hole recombination, or rather by charge-carrier selective processes such as charge extraction at collection layers or electron/hole-specific trapping. This distinction is enabled by TRMC and TRPL reflecting different semiconductor properties: TRMC measures the time-resolved change in photoconductivity (σ_{TRMC}), which is defined as the mobility-weighted sum of the photoexcited charge-carrier densities,[37]

$$\sigma_{TRMC} = e(\mu_e n_e + \mu_h n_h), \tag{1}$$

where e is the elementary charge, n_e and n_h are photoexcited densities of electrons and holes, and μ_e and μ_h are the respective mobilities. In contrast, the TRPL intensity (I_{TRPL}) originates from radiative bimolecular recombination and is proportional to the product of the electron and hole densities,[34]

$$I_{TRPL} \propto R_{eh} n_e n_h, \tag{2}$$

where R_{eh} is the radiative recombination rate constant.

We show here that imbalances that may occur between electrons and holes over time can be directly visualised by the ratio of I_{TRPL} and σ_{TRMC}^2 transients. According to the above equations, this ratio is given by:

$$\frac{I_{TRPL}}{\sigma_{TRMC}^2} \propto \frac{R_{eh} n_e n_h}{e^2(\mu_e n_e + \mu_h n_h)^2} = \begin{cases} \dfrac{R_{eh} n_e}{e^2 \mu_h^2 n_h} & \text{if } n_e \ll n_h \text{(case 1)} \\[2mm] \dfrac{R_{eh} n_h}{e^2 \mu_e^2 n_e} & \text{if } n_h \ll n_e \text{(case 2)} \\[2mm] \dfrac{R_{eh}}{e^2(\mu_e + \mu_h)^2} & \text{if } n_e = n_h \text{(case 3)} \end{cases}$$

$$\tag{3}$$

Here, case 1 and 2 represent scenarios of strong charge-carrier imbalance, *e.g.* following selective extraction or trapping of electrons (case 1) or holes (case 2), for which the remaining hole or electron conductivities dominate.[40] As eqn (3) reveals, under this scenario, $\dfrac{I_{TRPL}}{\sigma_{TRMC}^2}$ evolves with the ratio of the densities

associated with minority and majority charge carriers $\left(\frac{n_{\text{minority}}}{n_{\text{majority}}}\right)$, which will decline over time as further charge extraction or trapping occurs. In contrast, if no charge-carrier imbalances occur (case 3), $\frac{I_{\text{TRPL}}}{\sigma_{\text{TRMC}}^2}$ is a constant over time, indicating that electrons and holes recombine concurrently, typically through bimolecular radiative recombination. Therefore, any decay in the ratio $\frac{I_{\text{TRPL}}}{\sigma_{\text{TRMC}}^2}$ can visualise directly the presence of charge-carrier selective extraction from the perovskites layer into a charge transport layer, given that these typically exhibit low charge-carrier mobility and so do not contribute significantly to the conductivity.[41,42]

To visualise how such analysis reveals transient charge imbalances, we conducted numerical simulations that involve non-radiative and radiative recombination processes (see SI Note 2 for further details). Fig. 1c and d display the implications of a charge-carrier selective process on I_{TRPL} and σ_{TRMC}^2 and therefore $\frac{I_{\text{TRPL}}}{\sigma_{\text{TRMC}}^2}$. When charge extraction or trapping is low (Fig. 1c), I_{TRPL} and σ_{TRMC}^2 decay at the same rate, dominated by radiative electron–hole recombination and $\frac{I_{\text{TRPL}}}{\sigma_{\text{TRMC}}^2}$ is constant over time. However, in the case of strong charge extraction or a high species-specific trap density (Fig. 1d) the I_{TRPL} and σ_{TRMC}^2 transients diverge because suppression of one species significantly quenches TRPL while TRMC retains a longer-lived component originating from the conductivity of the remaining majority carriers. Such divergence between minority and majority charge-carrier densities leads to the simulated drop in $\frac{I_{\text{TRPL}}}{\sigma_{\text{TRMC}}^2}$ over time.

We further show in Fig. 1b how measured transients and the derived ratio $\frac{I_{\text{TRPL}}}{\sigma_{\text{TRMC}}^2}$ evolve over time for a $\text{FA}_{0.83}\text{Cs}_{0.17}\text{Pb}(\text{I}_{0.6}\text{Br}_{0.4})_3$ film. The film was deposited on a quartz (Q) substrate and a polymethylmethacrylate (PMMA) top layer served as an inert encapsulating layer to minimize degradation and any influence of the ambient atmosphere[9] (see fabrication details in Methods section and further optoelectronic and structural characterisation in the SI). This Q/Perov/PMMA stack does not support charge extraction and measurements were carried out under 530 nm pulsed excitation without significant halide segregation occurring. We find that the temporal evolution of I_{TRPL} and σ_{TRMC}^2 is indeed very similar, showing that trap-mediated recombination is minimal with at most minor contributions from shallow traps[43] (see SI Note 3) and recombination is largely governed by radiative bimolecular recombination, as would be expected for excitation densities near 10^{17} cm^{-3} given reported trap densities of $\sim 10^{15}$ cm^{-3} for typical lead halide perovskites.[34,44] The calculated ratio $\frac{I_{\text{TRPL}}}{\sigma_{\text{TRMC}}^2}$ is nearly constant, directly visualising the very minor charge imbalance in the high-quality perovskite film when no extraction layers are present.

Effect of halide segregation on charge-carrier mobility and recombination

We proceed by first establishing how light-induced halide segregation affects charge-carrier dynamics, after which we assess its influence on charge extraction in the next section. Halide segregation substantially alters the optoelectronic properties of mixed-halide perovskite even though the I-rich domains comprise only a small volume fraction,[8,27] because charge carriers generated in the mixed phase rapidly funnel into the photo-generated I-rich phase owing to its lower bandgap.[8] As a result, the evolution of halide segregation is often monitored by red-shifts in photoluminescence spectra. As Fig. 2a shows, continued illumination of a $\text{FA}_{0.83}\text{Cs}_{0.17}\text{Pb}(\text{I}_{0.6}\text{Br}_{0.4})_3$ film (Q/Perov/PMMA) over 6 hours indeed results in a gradual redshift of the original ssPL emission peak associated with the mixed-halide phase to a spectrum reflecting I-enriched domains. Similarly, Fig. 2b compares the film's absorption coefficient before (α_B) and after segregation (α_A), evidencing a broadening of the absorption, *i.e.* a decrease in α near the onset (reduction of original mixed phase) accompanied by an increase in α within the band-tail region (emergence of I-rich domains). The inset reveals the change in the absorption onset $(\Delta\alpha = \alpha_A - \alpha_B)$ during illumination, whose spectral integral

$$\left(\frac{\int_{E_1}^{E_2} \Delta\alpha \, dE}{\int_{E_1}^{E_2} (\alpha_A + \alpha_B)/2 \, dE} = 0.003\right)$$

is very low. Therefore, little change in overall absorption strength occurs, suggesting negligible degradation or material loss during phase segregation.

We next examine how halide segregation affects the charge-carrier mobility and recombination by concurrently recording TRPL transients for mixed-phase $(I_{\text{TRPL}}^{\text{Mixed}})$ and I-rich phase $(I_{\text{TRPL}}^{\text{I-rich}})$ emission, as well as the TRMC photoconductivity dynamics (σ_{TRMC}). Fig. 2c and d show how the TRPL transients for $I_{\text{TRPL}}^{\text{Mixed}}$ and $I_{\text{TRPL}}^{\text{I-rich}}$ evolve in the absence of a charge extraction layer (Q/Perov/PMMA). The initial amplitude of $I_{\text{TRPL}}^{\text{Mixed}}$ $(t = 0 \text{ ns})$ declines rapidly upon halide segregation, while that of $I_{\text{TRPL}}^{\text{I-rich}}$ $(t = 0 \text{ ns})$ is initially negligible but increases significantly (Fig. 2f), mirroring the red-shift observed in the ssPL (Fig. 2a). Moreover, the charge-carrier dynamics change substantially following halide segregation. For the mixed phase, segregation accelerates the decay of $I_{\text{TRPL}}^{\text{Mixed}}$ substantially (Fig. 2c) over the 6 hours of illumination, until it is limited by our instrument time resolution (<1 ns, see SI Note 4), consistent with a previous report of charge-carrier funnelling happening within tens of ps.[31] The TRMC (σ_{TRMC}) transients (Fig. 2e) on the other hand, reflect the dynamics of charge carriers irrespective of whether they are located in the mixed or iodide-rich phase. Following segregation, σ_{TRMC} exhibits an accelerated decay, caused by funnelling of charge-carriers into I-rich domains, discussed further below. Notably, the initial value of σ_{TRMC} at $t = 0$ ns only declines by about 20% throughout the 6 h CW illumination as shown in Fig. 2f suggesting that in the absence of extraction layers, the effective mobility of $\sum \varphi\mu = 24.5$ cm^2 V^{-1} s^{-1} (see SI Note 5) does not deteriorate substantially even after charge
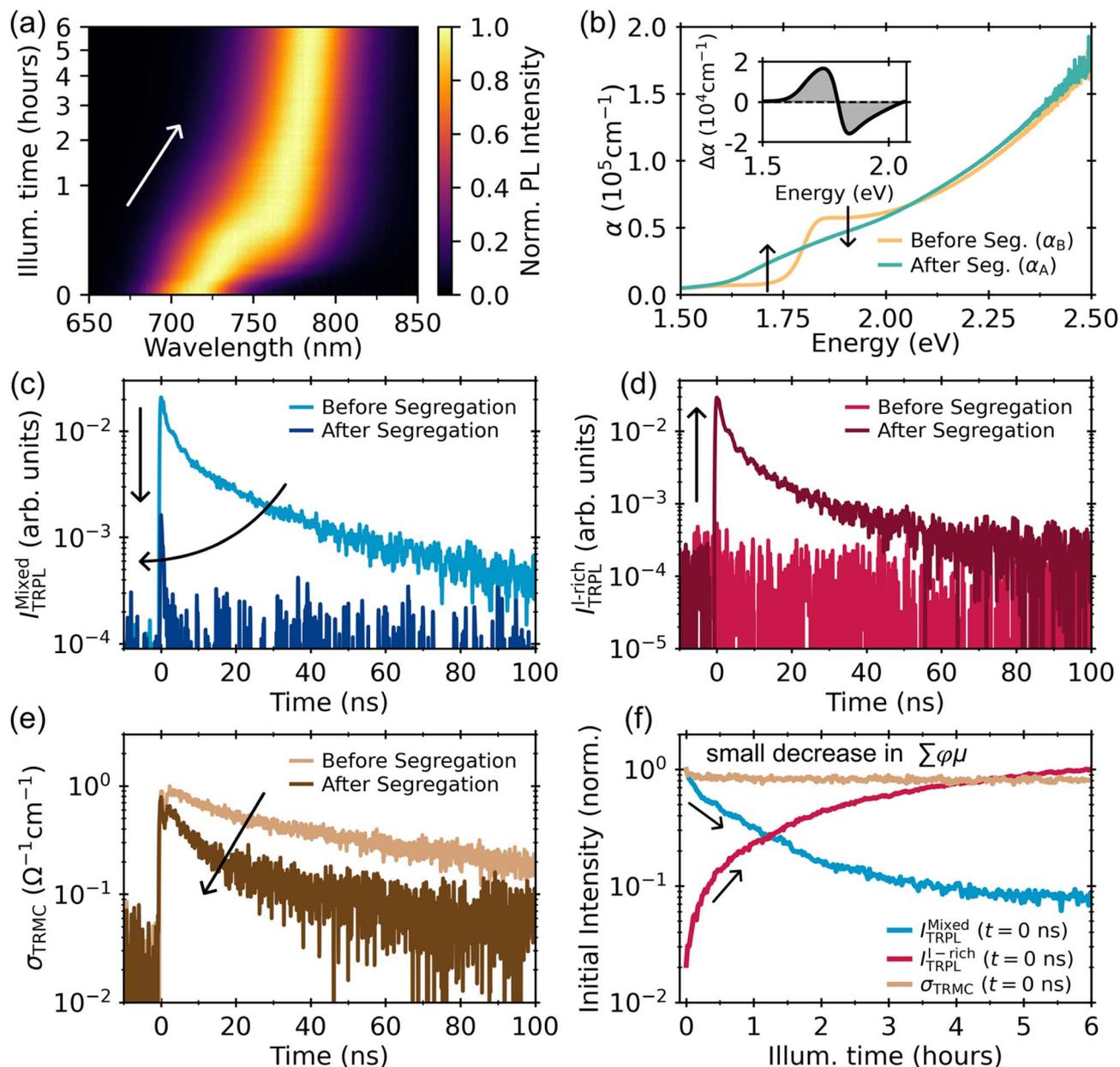
Fig. 2 (a) Normalised steady-state PL contour map recorded during 6 hours of continuous-wave illumination with 532 nm light of power density 150 mW cm^{-2} driving halide segregation. The illumination time is plotted on a square-root scale to highlight the early-time PL evolution. The relative increase in the PL intensity upon halide segregation is shown in Fig. S16. (b) Absorption spectra for Quartz(Q)/FA$_{0.83}$Cs$_{0.17}$Pb(I$_{0.6}$-Br$_{0.4}$)$_3$(perov)/PMMA before (α_B) and after halide segregation (α_A). The inset shows the change in the absorption spectra ($\Delta\alpha = \alpha_A - \alpha_B$) at the absorption edge. (c) Mixed-phase TRPL (I_{TRPL}^{Mixed}, 658–694 nm) and (d) I-rich phase TRPL (I_{TRPL}^{I-rich}, 800–850 nm) transients for Q/Perov/PMMA before and after halide segregation. (e) TRMC transients (σ_{TRMC}) for Q/Perov/PMMA before and after halide segregation. (f) Initial intensity value of transients, recorded at $t = 0$ ns after excitation, and plotted as a function of illumination time over 6 hours. $I_{TRPL}^{Mixed}(t = 0$ ns) and $\sigma_{TRMC}(t = 0$ ns) are normalised with respect to the value recorded when CW illumination commences (Illum. time = 0 h). $I_{TRPL}^{I-rich}(t = 0$ ns) values are normalised with respect to the value at 6 h illumination time. For panels (b)–(e), the label "before halide segregation" corresponds to 0 h of illumination, while "after segregation" corresponds to 6 h of illumination. For panels (c)–(f), Q/Perov/PMMA transients were recorded through pulsed excitation with a 530 nm laser at a pulse fluence of 3.6 μJ cm^{-2}. Arrows are included as visual guides to illustrate the evolution of relevant features during halide segregation. For Q/PTAA/Perov/PMMA and Q/SnO$_2$/Perov/PMMA, the ssPL and absorption changes during halide segregation are displayed in Fig S3–S6.

carriers have transferred into the I-rich phase. A similar preservation of charge-carrier mobilities after halide segregation has been reported at THz frequencies,[31] but here we find reasonable mobility retention even at microwave frequencies.

Given that the probed charge transport distance scales with the square root of the inverse probe frequency,[45] our 102 GHz probe has increased sensitivity to long-range defects and grain boundaries where halide segregation is known to dominantly

occur.[9,14,20,46,47] These results suggest that despite the charge-carrier localization, I-rich domains are relatively large, sufficiently spanning grains and grain boundaries[14,20,25,47,48] to permit sufficient free charge-carrier motion within these domains and potentially support charge extraction.[31] We attribute the modest mobility reduction to the slight geometric restrictions imposed within the percolation pathways generated by the continuum of I-rich domains. The size of such domains has been stipulated to range from 100 to 200 nm as observed by various microscopic techniques including cathodoluminescence[14] and STEM[47] which explains why such domain formation has a limited effect on charge transport. We can exclude the possibility of the reduction originating from intrinsic effects, given that iodide-rich lead halide perovskites have been shown to exhibit higher charge-carrier mobilities than bromide-rich perovskites.[34,49]

Effect of halide segregation on charge carrier extraction to transport layers

We further unravel how halide segregation affects charge extraction by investigating the effects on charge-carrier dynamics in half-stacks formed of $FA_{0.83}Cs_{0.17}Pb(I_{0.6}Br_{0.4})_3$ with commonly used charge transport materials. For this purpose, we deposited films of the perovskite on films of either PTAA or SnO_2 on quartz substrates and a PMMA layer was deposited on top to minimise permanent light-induced degradation.[50–52] Steady-state PL, XRD, and absorption measurements confirm the formation of the intended nominal composition of $FA_{0.83}Cs_{0.17}Pb(I_{0.6}Br_{0.4})_3$ on these layers (see Fig S2–S7). Fig. 3 reveals the effect of halide segregation on charge-carrier dynamics in such half-stacks, with the three columns representing Q/Perovskite/PMMA, Q/PTAA/Perovskite/PMMA and Q/SnO$_2$/Perovskite/PMMA architectures, and the three rows the TRPL transients, squared TRMC transients and their ratio. We note that to examine the effect of halide segregation on PL transients, we compare the TRPL transients of the original mixed phase (I_{TRPL}^{Mixed}) before segregation with those of the I-rich phase (I_{TRPL}^{I-rich}) after segregation, because, as discussed above, funnelling is so rapid that recombination predominantly occurs in these two different phases before and after segregation, respectively (see SI Note 4). Importantly, regardless of whether or not an extraction layer is present, both TRPL and
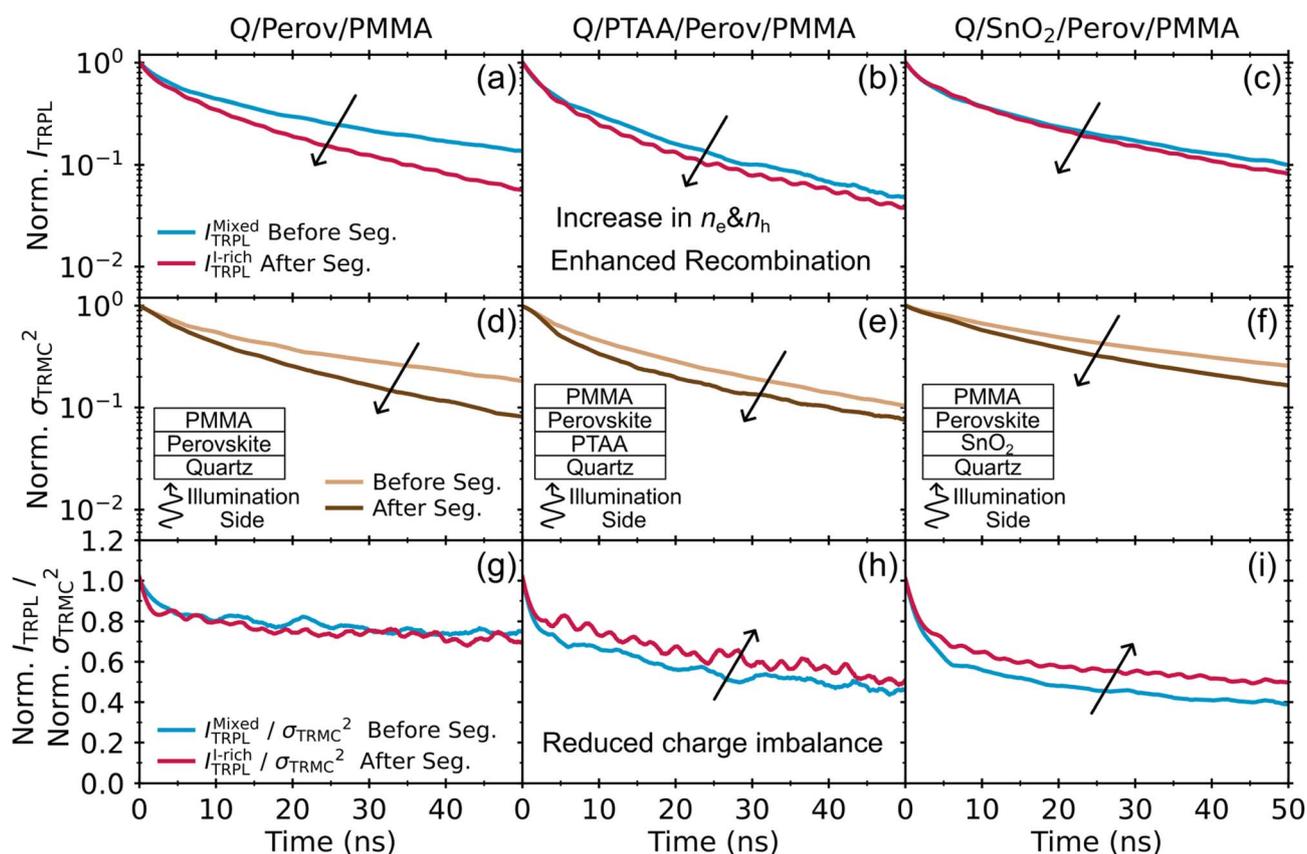

Fig. 3 (a)–(c) Normalised mixed-phase TRPL transients (I_{TRPL}^{Mixed}) before halide segregation had commenced (blue) compared with I-rich phase TRPL transients (I_{TRPL}^{I-rich}) after 6 hours of halide segregation (red), shown for (a) Quartz(Q)/FA$_{0.83}$Cs$_{0.17}$Pb(I$_{0.6}$Br$_{0.4}$)$_3$(Perov)/PMMA, (b) Q/PTAA/Perov/PMMA, and (c) Q/SnO$_2$/Perov/PMMA. (d)–(f) Normalised squared TRMC photoconductivity transients (σ_{TRMC}^2) before (light brown) and after halide segregation for 6 h (dark brown) for the same device stacks as in (a)–(c). The insets show the thin-film architectures and the illumination direction (arrow) from the quartz substrate near the charge transport layers. We use a 530 nm pulsed excitation at the fluence of 3.6 μJ cm^{-2} for transients and 530 nm CW illumination at the power density of 150 mW cm^{-2} to induce halide segregation. (g)–(i) Ratio of normalised mixed phase TRPL transient to the square of the normalised TRMC photoconductivity ($I_{TRPL}^{Mixed}/\sigma_{TRMC}^2$) before (blue) and after (red) halide segregation. The method to extract the ratio is detailed in SI Note 6. Legends are shared horizontally across panels (a)–(c), (d)–(f) and (g)–(i).

squared TRMC (σ_{TRMC}^2) transients clearly show that halide segregation causes an accelerated decay of the charge-carrier density. We attribute this effect to the enhanced radiative electron–hole recombination owing to an increase in charge-carrier density following funnelling into the I-rich domains which only cover a fraction of perovskite film volume, as evidenced by the corresponding increase in steady-state photoluminescence intensity upon segregation (Fig. S16).[8,31] We exclude the possibility of this effect being caused by any increase in the bimolecular recombination rate constant between the mixed-phase and I-rich phases, because the rate constant has instead been shown to decrease with increasing iodide fraction in $FA_{0.83}Cs_{0.17}Pb(I_{1-x}Br_x)_3$.[34,49]

We further probe the effect of halide segregation on charge extraction at the interface of the perovskite with PTAA or SnO$_2$. To isolate the effects of charge-selective processes occurring at the perovskite interface from those caused by accelerated radiative recombination, we calculate the transient ratio of $\frac{I_{TRPL}}{\sigma_{TRMC}^2}$, presented in the bottom row of Fig. 3, which reveals any evolving imbalance between electron and hole densities, as discussed above. While electrons and holes are initially photogenerated in equal numbers, transfer or trapping of either only electrons or only holes is expected to lead to a decay of $\frac{I_{TRPL}}{\sigma_{TRMC}^2}$ over time. This method thus allows us to qualitatively discuss the effect of such charge selective processes without having to solve multi-parameterised coupled differential equations or computationally expensive drift-diffusion model on charge-carrier dynamics before and after halide segregation.[34,44,53–56] This simplification is particularly valuable because halide segregation likely induces a distribution of I-rich phases rather than a simple two-phase system employed in other studies,[31] further complicating such models.

The $\frac{I_{TRPL}}{\sigma_{TRMC}^2}$ transients (bottom row, Fig. 3) indeed reveal clear evidence for charge extraction in the presence of either PTAA or SnO$_2$ extraction layers. In the absence of such extraction layers (Q/Perov/PMMA reference stack, Fig. 3g) the $\frac{I_{TRPL}}{\sigma_{TRMC}^2}$ ratio decays relatively little, both before and after halide segregation, indicating only minor effect of charge-selective trapping, consistent with high-quality film material and interfaces (see SI Note 3). We note that halide segregation causes little change to these transients because any acceleration of bimolecular electron–hole recombination owing to the increase in the charge-carrier density is cancelled out in the division of the I_{TRPL} and σ_{TRMC}^2 transients (Case 3 in eqn (3)), indicating that halide segregation induces negligible change in trap-mediated recombination. In contrast, when charge transport layers are introduced (Fig. 3h and i), $\frac{I_{TRPL}}{\sigma_{TRMC}^2}$ transients exhibit a clear initial decay within 10 ns followed by a slow component, evidencing charge-selective processes associated with these new interfaces. Given that similar dynamics are observed irrespective of the type of charge transport layer, we attribute the fast early decay to charge extraction rather than enhanced

charge-carrier trapping.[34,57] Importantly, following halide segregation, these $\frac{I_{TRPL}}{\sigma_{TRMC}^2}$ ratios still exhibit the fast decline associated with charge extraction. Given that the PL and conductivity in this case originate from charge carriers located in the I-rich phase, these transients clearly show that charge-extraction is still eminently feasible even after charge carriers have been funnelled into these domains.

Fig. 3h and i also reveal that after six hours of segregation, the charge-carrier imbalance is less pronounced for Q/PTAA/Perov/PMMA and Q/SnO$_2$/Perov/PMMA, as evidenced by the increased amplitude of slow late-time decay of the ratio of $I_{TRPL}^{I\text{-rich}}/\sigma_{TRMC}^2$. We attribute this behaviour to enhanced charge-carrier back transfer from charge transport layer to the I-rich phase owing to more favourable energy-level alignment compared with the original mixed phase.[10,34] Such enhancement in back transfer partly alleviates the lifetime reduction otherwise caused by enhanced bimolecular radiative recombination owing to charge-carrier funnelling (see SI Note 7 for further discussion). Overall, these findings indicate that despite extensive phase segregation occurring in the perovskite films, surprisingly effective percolation pathways are maintained towards the charge-extraction layers.[16]

Projected impact of halide segregation on photovoltaic performance

Overall, our findings show that halide segregation leaves charge-carrier mobility and extraction pathways relatively intact, but significantly accelerates bimolecular, radiative electron–hole recombination. Fig. 4 illustrates the changes occurring in the dynamical processes following halide segregation for the three half-stack configurations. In the absence of charge extraction layers (Q/Perov/PMMA) and prior to any segregation (Fig. 4a), charge carriers recombine in accordance with a typical rate equation model involving radiative electron–hole recombination (R_{eh}) and through population (R_{pop}), depopulation (R_{depop}) and release from traps (k_{detrap}) (see SI Notes 2 and 3). However, halide segregation (Fig. 4b) bypasses these processes by rapid funnelling of charge carriers into the I-rich phase, which only occupies a smaller sub-volume of the film.[8] This funnelling thus leads to a local increase in charge-carrier density, causing accelerated radiative emission (eqn (2)). Once charge-extraction layers are introduced (Fig. 4c and e) additional dynamic processes associated with the interface occur, such as charge transfer, back transfer and interfacial recombination.[34] However, following halide segregation (Fig. 4d and f), charge-carrier funnelling to the I-rich phase occurs much more rapidly than charge extraction from the mixed phase. Therefore, any transfer into either PTAA or SnO$_2$ must now be accomplished from the I-rich phase and it still surprisingly effective.

To evaluate the projected impact of halide segregation on the short-circuit current density J_{SC} we further examine changes in the charge-carrier diffusion length (L_D), which is proportional to the square root of the total recombination rate (τ) and the charge-carrier mobility (μ). We evaluate the mobility from the value of σ_{TRMC} immediately following excitation, and the
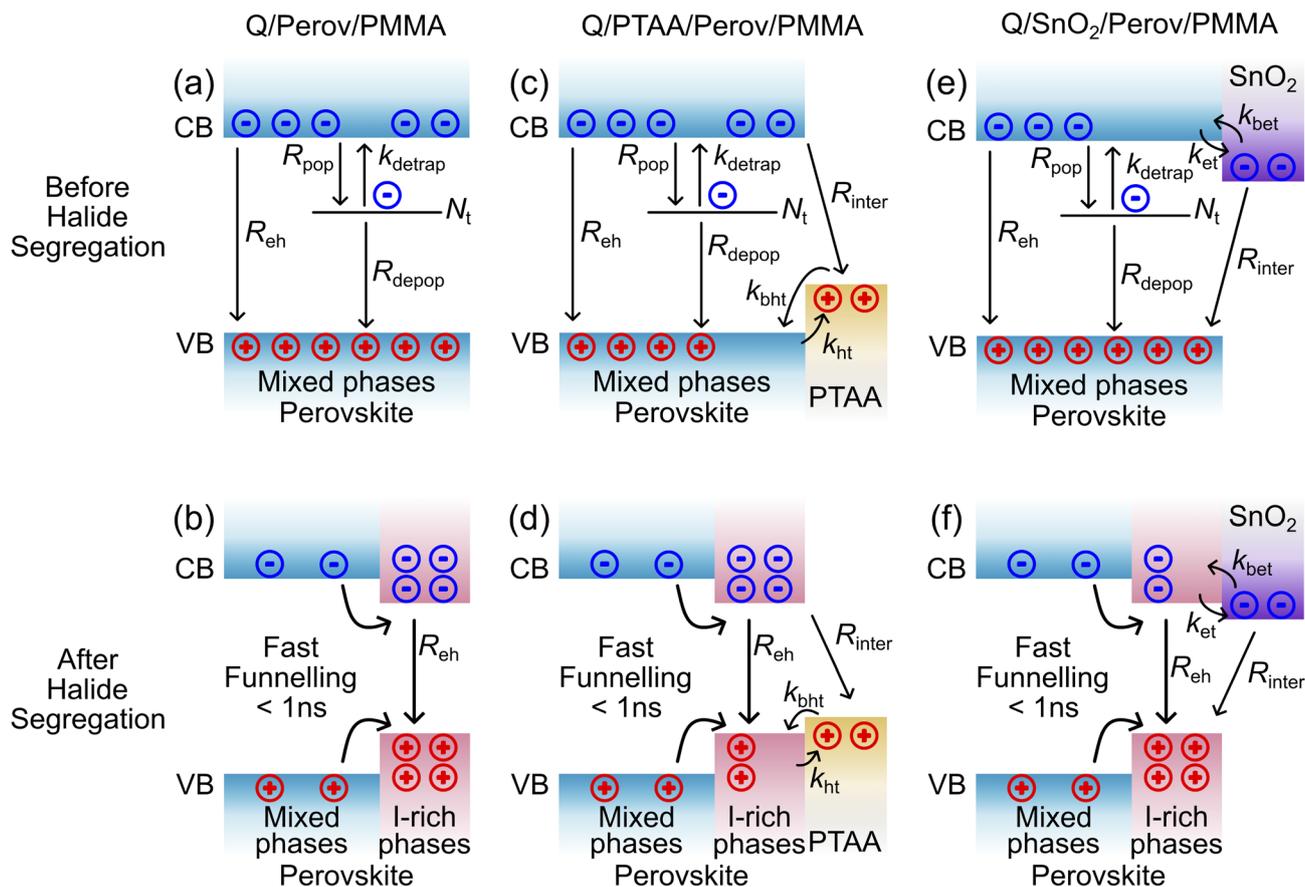
Fig. 4 (a) and (b) Schematic illustration of charge-carrier dynamics in Quartz(Q)/FA$_{0.83}$Cs$_{0.17}$Pb(I$_{0.6}$Br$_{0.4}$)$_3$(Perov)/PMMA before and after halide segregation respectively, showing radiative bimolecular recombination (R_{eh}) and the non-radiative trap-mediated recombination processes, which are trap population (R_{pop}), detrapping (k_{detrap}) and depopulation (R_{depop}). The blue region represents conduction band (CB) and valence and (VB) of the mixed phase with blue minus and red plus symbols corresponding to electrons and holes respectively. (c)–(d) Schematics of charge-carrier dynamics in the presence of PTAA before and after halide segregation respectively, including additional interfacial processes such as hole transfer (k_{ht}), hole back transfer (k_{bht}) and interfacial recombination (R_{inter}). The yellow region indicates the highest occupying molecular orbital (HOMO) of PTAA. (e)–(f) Schematic illustration of charge-carrier dynamics in the presence of SnO$_2$ before and after halide segregation respectively with electron transfer (k_{et}) and back transfer (k_{bet}) and R_{inter}. The purple region represents the CB of SnO$_2$.

lifetime from the subsequent decay of the transients shown in Fig. 3 (see Table S6 for values and SI Note 8 for further explanations). By evaluating these parameters both before and after halide segregation across the three stacks, we find that segregation causes the diffusion length to decline by about 35%, which will suppress charge collection and therefore J_{SC}.[58] This is consistent with full device data showing reduction in J_{SC} upon halide segregation.[25,28,30] We note that under full device operation, the charge-collection efficiency might be influenced by additional factors such as mobile ion-induced field screening.[59] However, our results clearly demonstrate that the combined effects of enhanced radiative recombination and reduction in mobility contribute to limiting charge-carrier collection efficiency upon halide segregation in the presence of charge transport layers.

In addition, we consider changes occurring in the open-circuit voltage V_{OC} following halide segregation. Here, two counteracting factors are at play. A clear loss in V_{OC} should be expected given that charge carriers funnel from the original

higher-energy FA$_{0.83}$Cs$_{0.17}$Pb(I$_{0.6}$Br$_{0.4}$)$_3$ mixed-halide phase into a lower-energy iodide-enriched phase. Mahesh *et al.* indeed experimentally observed a 75 mV V_{OC} loss upon segregation for a photovoltaics devices based on the same perovskite composition used here. However, this value is smaller than the 97 mV penalty predicted by detailed-balance calculations ignoring charge-carrier funnelling effects.[27] Such V_{OC} compensation of a few tens of meV most likely arises from the enhanced radiative efficiency associated with the charge-carrier funnelling observed in our study (see SI Note 9 for further discussions) which will increase quasi Fermi-level splitting (QFLS). Although V_{OC} losses following halide segregation have primarily been attributed to non-radiative recombination, recent advances in additive engineering and novel transport layers have substantially mitigated such loss channels,[60–63] likely making the emergence of low-bandgap iodide-rich domains a dominant factor. However, it is worth noting that for the ideal scenario of a nearly trap-free mixed halide perovskite with nearly unity PLQY, enhanced radiative rates induced by halide segregation

cannot provide significant V_{OC} compensation. In this regime, bimolecular recombination no longer competes with trap-mediated recombination, so the achievable V_{OC} becomes intrinsically limited by the difference in the radiative QFLS limits of the mixed and I-rich phases (see SI Note 9). That said, such highly-performing devices based on advanced passivation methods or compositional engineering also typically exhibit reduced halide segregation in the first place.[22,60,61,64–68] Overall, our considerations explain why halide segregation may cause the widely reported losses in either V_{OC}, J_{SC} or both quantities,[25,27–30] and so an overall decline in power conversion efficiency of the solar cell.

In conclusion, we have demonstrated how halide segregation fundamentally alters charge-carrier dynamics in wide-bandgap mixed-halide perovskites interfaced with charge-transport layers. Using synchronous multimodal spectroscopy that combines TRMC, TRPL and ssPL, we reveal that halide segregation drives sub-nanosecond funnelling of charge-carriers into the I-rich domains, where enhanced radiative recombination directly competes with charge extraction. This acceleration in radiative electron–hole recombination, as well as a slight reduction in mobilities measured at microwave frequencies, reduces charge diffusion length by approximately 35%. We find that these effects are alleviated somewhat by counteracting effects, such as an enhancement in radiative efficiency and stronger charge-carrier back transfer resulting from more favourable energy-level alignment between the iodide-rich perovskites and the charge transport layer. However, we show that the overall effect on photovoltaic device efficiencies is expected to be detrimental. These insights establish a direct link between halide segregation and the widely observed V_{OC} and J_{SC} losses in wide-bandgap perovskite solar cells. Importantly, our free-space multimodal approach provides a powerful diagnostic to disentangle radiative and interfacial processes, which cannot be resolved by TRMC or TRPL alone. Overall, our study highlights the need for strategies that either suppress halide segregation or mitigate the adverse effect of charge-carrier funnelling to enable efficient integration of stable wide-bandgap mixed-halide perovskites into multi-junction solar cells.

Methods

Materials

Tin(IV) oxide (SnO$_2$, 15% in H$_2$O colloidal dispersion) was purchased from Alfa Aesar and was diluted to 2% with deionised water. PTAA (poly[bis(4-phenyl)(2,4,6-trimethylphenyl) amine) was purchased from Flexink and was dissolved in chlorobenzene (Sigma) at a concentration of 2.0 mg mL^{-1}. PMMA (poly(methyl methacrylate), Sigma-Aldrich, mean molar weight 97 000 g mol^{-1}) was dissolved in chlorobenzene (Sigma-Aldrich) at 150 mg mL^{-1}.

The FA$_{0.83}$Cs$_{0.17}$Pb(I$_{0.6}$Br$_{0.4}$)$_3$ perovskite precursor solution was obtained by stoichiometrically weighing formamidinium iodide (FAI, GreatCell Solar), cesium iodide (CsI, AlfaAesar), lead iodide (PbI$_2$, TCI) and lead bromide (PbBr$_2$, AlfaAesar) in a N$_2$ filled glovebox. The precursor salts were dissolved in

a mixture (4 : 1 ratio by volume) of dimethylformamide (DMF) and dimethylsulfoxide (DMSO) at a concentration of 1.2 M which was stirred overnight with no heating. The solution was used with no further steps.

Deposition protocols

The z-cut quartz substrates (UQG Optics, 13 mm diameter, 2 mm thickness) were cleaned by subsequent sonication in Hellmanex (3% in deionised water), deionised water, acetone and isopropanol for 15 minutes. The substrates were then treated with UV-Ozone for 15 minutes after which they were transferred into a N$_2$ filled glovebox (except the SnO$_2$ deposition)

SnO$_2$: The SnO$_2$ solution was spin-coated in ambient air onto quartz substrates at a spin rate of 4000 rpm for 30 s. The substrates were then annealed at 180 °C for 30 min in air. Before spinning the perovskite layer, the substrates were treated with UV-ozone for 10 minutes and then transferred into a N$_2$-filled glovebox.

PTAA: the PTAA solution was spincoated by depositing 50 μL of solution onto the quartz substrates spinning at 6000 rpm for 30 s. The substrates were annealed for 10 min at 100 °C. This layer was treated with a solution of Al$_2$O$_3$ nanoparticles diluted at 1 : 150 by volume in isopropanol, deposited at 2000 rpm for 20 s and annealed for 30 s to improve wetting and ensure full film coverage.

FA$_{0.83}$Cs$_{0.17}$Pb(I$_{0.6}$Br$_{0.4}$)$_3$ Perovskite: onto z-cut quartz substrates, 50 μL of the precursor solution was dynamically deposited onto the substrate spinning at 1000 rpm. After 5 s, the spin speed increased to 5000 rpm over 5 s, where it remained for 30 s. An antisolvent quench was performed by depositing 50 μL of anisole onto the substrate 5 s before the end of the program. The films were annealed for 60 minutes at 100 °C.

PMMA: a PMMA layer was deposited to encapsulate the samples, minimising atmospheric effects. To form the PMMA film, 40 μL of solution was deposited statically onto the perovskite film which was accelerated to 2000 rpm at a rate of 1000 rpm s^{-1}. The spin coating duration was 25 s. The films were then annealed at 100 °C for 3 min to drive off any residual solvent.

Synchronous multimodal spectroscopy of TRMC, TRPL and ssPL

Microwave radiation at 34 GHz was generated using a signal generator, converted to 102 GHz using a frequency tripler, and launched into free space with a standard gain feed horn antenna. The high-frequency, millimeter-wave microwave radiation was focused onto a sample and re-focused onto a detector with PTFE lenses. The microwave field transmitted through the sample was measured with a custom-made GaAs Schottky-diode detector and measured with a fast oscilloscope (Tektronix MSO64). The microwave conductivity system was operated in transmission geometry with most of the incident microwave signal being transmitted through the sample, and the change in transmission directly upon photoexcitation typically amounting

to <5% of the transmitted signal in the absence of photoexcitation, depending on the excitation fluence used. The mixed and I-rich phase TRPL were measured using 658–694 nm (Edmund Optics, #86-988) and 800–850 nm (Edmund Optics, #86-95) bandpass filters respectively with a fast photodiode detector (Thorlabs, DET025A/M), from which the signal was amplified with a broad-band amplifier made in-house and measured with the same oscilloscope as above. The spectrally resolved photoluminescence was measured using a fibre-coupled spectrometer (Ocean Optics, SR6) with 600 nm long-pass filter (Thorlabs, FELH0600) to filter out the excitation laser peak. The steady-state photoluminescence spectra are spectrally corrected with an OL245M irradiance standard tungsten lamp and background-corrected by a spectrum recorded without laser excitation for the same acquisition time. The samples were photoexcited with pulsed laser light originating from a Ti:Sapphire amplified laser system (Spectra-Physics, MaiTai-Ascend-Spitfire, 35 fs pulse duration), converted to 530 nm central wavelength using an optical parametric amplifier (Light Conversion, TOPAS-C). The 532 nm background CW light was generated by a Ventus 532 laser.

Absorption spectroscopy

Reflectance (R) and transmittance (T) spectra were measured using a Fourier transform infrared (FTIR) spectrometer (Bruker VERTEX 80v), configured with a tungsten halogen lamp illumination source, a CaF_2 beamsplitter and a silicon diode detector. Absorbance (A) is calculated with the following equation:

$$A = -\ln\left(\frac{T}{1-R}\right) \qquad (4)$$

The absorption coefficient (α) spectra were calculated by dividing A by the film thicknesses shown in Table S1.

X-ray diffraction

The X-ray diffraction (XRD) patterns were measured in air using a Panalytical Empyrean powder diffractometer with a copper X-ray source (Cu Kα_1 X-rays with a wavelength of 1.5406 Å). The scan range was from 10.0° to 45.0° and the scan step size was set as 0.004°. The raw XRD patterns were then corrected for tilt by shifting the 2θ-axis to the z-cut quartz reference peak, which is at 2θ = 16.433°.[69]

Author contributions

J. E. L. and L. M. H. conceived the idea and designed the experiments. J. E. L. conducted absorption, XRD and the synchronous multimodal spectroscopy measurements. R. D. J. O. fabricated the perovskite films. J. R. S. L., A. M. U. and M. B. J. contributed to the measurement and development of the synchronous multimodal spectroscopy measurements. R. S. and A. J. R. conducted AFM measurements. J. E. L. wrote the first draft of the manuscript. L. M. H. supervised the project. All authors discussed the results and reviewed the manuscript.

Conflicts of interest

Henry Snaith is cofounder and CSO of Oxford PV Ltd, a company commercializing perovskite PV technology.

Data availability

The data supporting this article have been included as part of the supplementary information (SI). Supplementary information: PL spectra before and after segregation, absorption spectra before and after segregation, XRD patterns, synchronous multimodal spectroscopy transient data, AFM measurement data, charge-carrier density calculations for synchronous multimodal spectroscopy, numerical simulation models and parameters used in this work, mobility calculations from TRMC, data processing methods for I_{TRPL}/σ_{TRMC}^2 ratio, detailed explanation of trends in the ratio of I_{TRPL}/σ_{TRMC}^2 after segregation, calculation of diffusion length ratio, calculation of change in the quasi-Fermi level splitting, bimolecular radiative recombination constant calculations from OPTP. See DOI: https://doi.org/10.1039/d6el00003g.

Acknowledgements

References

1 NREL, Best Research-Cell Efficiency Chart, https://www.nrel.gov/pv/cell-efficiency.html, 2026.

2 L. Jia, S. Xia, J. Li, Y. Qin, B. Pei, L. Ding, J. Yin, T. Du, Z. Fang, Y. Yin, J. Liu, Y. Yang, F. Zhang, X. Wu, Q. Li, S. Zhao, H. Zhang, Q. Li, Q. Jia, C. Liu, X. Gu, B. Liu, X. Dong, J. Liu, T. Liu, Y. Gao, M. Yang, S. Yin, X. Ru, H. Chen, B. Yang, Z. Zheng, W. Zhou, M. Dou, S. Wang, S. Gao, L. Chen, M. Qu, J. Lu, L. Fang, Y. Wang, H. Deng, J. Yu, X. Zhang, M. Li, X. Lang, C. Xiao, Q. Hu, C. Xue, L. Ning, Y. He, Z. Li, X. Xu and B. He, *Nature*, 2025, **644**, 912–919.

3 M. T. Hörantner, T. Leijtens, M. E. Ziffer, G. E. Eperon, M. G. Christoforo, M. D. McGehee and H. J. Snaith, *ACS Energy Lett.*, 2017, **2**, 2506–2513.

4 G. Eperon, H. Snaith and M. Hoerantner, *Nat. Rev. Chem.*, 2017, **1**, 0095.

5 M. H. Futscher and B. Ehrlerm, *ACS Energy Lett.*, 2016, **1**, 863–868.

6 D. P. McMeekin, G. Sadoughi, W. Rehman, G. E. Eperon, M. Saliba, M. T. Hörantner, A. Haghighirad, N. Sakai, L. Korte, B. Rech, M. B. Johnston, L. M. Herz and H. J. Snaith, *Science*, 2016, **351**, 151–155.

7 S. Tao, I. Schmidt, G. Brocks, J. Jiang, I. Tranca, K. Meerholz and S. Olthof, *Nat. Commun.*, 2019, **10**, 10.

8 E. T. Hoke, D. J. Slotcavage, E. R. Dohner, A. R. Bowring, H. I. Karunadasa and M. D. McGehee, *Chem. Sci.*, 2015, **6**, 613–617.

9 A. J. Knight, A. D. Wright, J. B. Patel, D. P. McMeekin, H. J. Snaith, M. B. Johnston and L. M. Herz, *ACS Energy Lett.*, 2019, **4**, 75–84.

10 V. J.-Y. Lim, A. J. Knight, R. D. J. Oliver, H. J. Snaith, M. B. Johnston and L. M. Herz, *Adv. Funct. Mater.*, 2022, **32**, 2204825.

11 Z. Chen, G. Brocks, S. Tao and P. A. Bobbert, *Nat. Commun.*, 2021, **12**, 2687.

12 S. Draguta, O. Sharia, S. J. Yoon, M. C. Brennan, Y. V. Morozov, J. S. Manser, P. V. Kamat, W. F. Schneider and M. Kuno, *Nat. Commun.*, 2017, **8**, 200.

13 X. Wang, Y. Ling, X. Lian, Y. Xin, K. B. Dhungana, F. Perez-Orive, J. Knox, Z. Chen, Y. Zhou, D. Beery, K. Hanson, J. Shi, S. Lin and H. Gao, *Nat. Commun.*, 2019, **10**, 695.

14 C. G. Bischak, C. L. Hetherington, H. Wu, S. Aloni, D. F. Ogletree, D. T. Limmer and N. S. Ginsberg, *Nano Lett.*, 2017, **17**, 1028–1033.

15 A. J. Barker, A. Sadhanala, F. Deschler, M. Gandini, S. P. Senanayak, P. M. Pearce, E. Mosconi, A. J. Pearson, Y. Wu, A. R. S. L. Kandada, T. Leijtens, F. D. Angelis, S. E. Dutton, A. Petrozza and R. H. Friend, *ACS Energy Lett.*, 2017, **2**, 1416–1424.

16 A. J. Knight, J. B. Patel, H. J. Snaith, M. B. Johnston and L. M. Herz, *Adv. Energy Mater.*, 2020, **10**, 11.

17 T. Elmelund, B. Seger, M. Kuno and P. V. Kamat, *ACS Energy Lett.*, 2020, **5**, 56–63.

18 I. M. Pavlovetc, A. Ruth, I. Gushchina, L. Ngo, S. Zhang, Z. Zhang and M. Kuno, *ACS Energy Lett.*, 2021, **6**, 2064–2071.

19 Y. Zhou, Y.-H. Jia, H.-H. Fang, M. A. Loi, F.-Y. Xie, L. Gong, M.-C. Qin, X.-H. Lu, C.-P. Wong and N. Zhao, *Adv. Funct. Mater.*, 2018, **28**, 1803130.

20 N. Phung, A. Al-Ashouri, S. Meloni, A. Mattoni, S. Albrecht, E. L. Unger, A. Merdasa and A. Abate, *Adv. Energy Mater.*, 2020, **10**, 1903735.

21 D. Kim, J. Lim, S. Lee, A. M. Soufiani, E. Choi, A. V. Ievlev, N. Borodinov, Y. Liu, O. S. Ovchinnikova, M. Ahmadi, S. Lim, P. Sharma, J. Seidel, J. H. Noh and J. S. Yun, *ACS Nano*, 2021, **15**, 20391–20402.

22 A. J. Knight, J. Borchert, R. D. J. Oliver, J. B. Patel, P. G. Radaelli, H. J. Snaith, M. B. Johnston and L. M. Herz, *ACS Energy Lett.*, 2021, **6**, 799–808.

23 W. Mao, C. R. Hall, S. Bernardi, Y.-B. Cheng, A. Widmer-Cooper, T. A. Smith and U. Bach, *Nat. Mater.*, 2021, **20**, 55–61.

24 R. D. J. Oliver, P. Caprioglio, F. peña-Camargo, L. R. V. Buizza, F. Zu, A. J. Ramadan, S. G. Motti, S. Mahesh, M. M. McCarthy, J. H. Warby, Y.-H. Lin, N. Koch, S. Albrecht, L. M. Herz, M. B. Johnston, D. Neher, M. Stolterfoht and H. J. Snaith, *Energy Environ. Sci.*, 2022, **15**, 714–726.

25 Y. Guo, C. Zhang, L. Wang, X. Yin, B. Sun, C. Wei, X. Luo, S. Yang, L. Sun and B. Xu, *Energy Environ. Sci.*, 2025, **18**, 2308–2317.

26 J. R. S. Lilly, V. J. Y. Lim, J. B. Patel, S. Yan, J. E. Lee, M. B. Johnston and L. M. Herz, *Small Struct.*, 2025, **7**, e202500545.

27 S. Mahesh, J. M. Ball, R. D. J. Oliver, D. P. McMeekin, P. K. Nayak, M. B. Johnston and H. J. Snaith, *Energy Environ. Sci.*, 2020, **13**, 258.

28 K. Datta, B. T. van Gorkom, Z. Chen, M. J. Dyson, T. P. A. van der Pol, S. C. J. Meskers, S. Tao, P. A. Bobbert, M. M. Wienk and R. A. J. Janssen, *ACS Appl. Energy Mater.*, 2021, **4**, 6650–6658.

29 K. A. Bush, K. Frohna, R. Prasanna, R. E. Beal, T. Leijtens, S. A. Swifter and M. D. McGehee, *ACS Energy Lett.*, 2018, **3**, 428–435.

30 J. Wen, Y. Zhao, P. Wu, Y. Liu, X. Zheng, R. Lin, S. Wan, K. Li, H. Luo, Y. Tian, L. Li and H. Tan, *Nat. Commun.*, 2023, **14**, 7118.

31 S. G. Motti, J. B. Patel, R. D. J. Oliver, H. J. Snaith, M. B. Johnston and L. M. Herz, *Nat. Commun.*, 2021, **12**, 6955.

32 K. Suchan, T. J. Jacobsson, C. Rehermann, E. L. Unger, T. Kirchartz and C. M. Wolff, *Adv. Energy Mater.*, 2023, **14**, 2303420.

33 P. Caprioglio, J. A. Smith, R. D. J. Oliver, A. Dasgupta, S. Choudhary, M. D. Farrar, A. J. Ramadan, Y.-H. Lin, M. G. Christoforo, J. M. Ball, J. Diekmann, J. Thiesbrummel, K.-A. Zaininger, X. Shen, M. B. Johnston, D. Neher, M. Stolterfoht and H. J. Snaith, *Nat. Commun.*, 2023, **14**, 932.

34 J. E. Lee, S. G. Motti, R. D. J. Oliver, S. Yan, H. J. Snaith, M. B. Johnston and L. M. Herz, *Adv. Funct. Mater.*, 2024, **34**, 2401052.

35 J. Endres, M. Kulbak, L. Zhao, B. P. Rand, D. Cahen, G. Hodes and A. Kahn, *J. Appl. Phys.*, 2017, 121.

36 M. Karmaoui, A. B. Jorge, P. F. McMillan, A. E. Aliev, R. C. Pullar, J. A. Labrincha and D. M. Tobaldi, *ACS Omega*, 2018, **3**, 13227–13238.

37 A. M. Ulatowski, K. A. Elmestekawy, J. B. Patel, N. K. Noel, S. Yan, H. Kraus, P. G. Huggard, M. B. Johnston and L. M. Herz, *Adv. Funct. Mater.*, 2023, **33**, 2305283.

38 F. D. Elhorst, J. E. Sebastián Alonso, H. J. Bolink and L. J. A. Koster, *ACS Energy Lett.*, 2025, 4574–4579.

39 E. V. Péan, J. Zhao, A. J. Doolin, R. García-Rodríguez, T. J. Savenije and M. L. Davies, *Small Methods*, 2025, 2400818.

40 W. Li, Q. Yuan, Y. Chen, J. R. S. Lilly, M. R. Filip, L. M. Herz, M. B. Johnston and J. Etheridge, *Adv. Mater.*, 2025, **37**, 2501788.

41 F. M. Rombach, S. A. Haque and T. J. Macdonald, *Energy Environ. Sci.*, 2021, **14**, 5161–5190.

42 P. Tiwana, P. Docampo, M. B. Johnston, H. J. Snaith and L. M. Herz, *ACS Nano*, 2011, **5**, 5158–5166.

43 Y. Yuan, G. Yan, C. Dreessen, T. Rudolph, M. Hülsbeck, B. Klingebiel, J. Ye, U. Rau and T. Kirchartz, *Nat. Mater.*, 2024, **23**, 391–397.

44 M. J. Trimpl, A. D. Wright, K. Schutt, L. R. V. Buizza, Z. Wang, M. B. Johnston, H. J. Snaith, P. Müller-Buschbaum and L. M. Herz, *Adv. Funct. Mater.*, 2020, **30**, 2004312.

45 L. A. Muscarella, E. M. Hutter, S. Sanchez, C. D. Dieleman, T. J. Savenije, A. Hagfeldt, M. Saliba and B. Ehrler, *J. Phys. Chem. Lett.*, 2019, **10**, 6010–6018.

46 X. Tang, M. van den Berg, E. Gu, A. Horneber, G. J. Matt, A. Osvet, A. J. Meixner, D. Zhang and C. J. Brabec, *Nano Lett.*, 2018, **18**, 2172–2178.

47 Q. Fan, Y. Cui, Y. Li, J. A. Vigil, Z. Jiang, P. Nandi, R. Colby, C. Zhang, H. I. Karunadasa and A. M. Lindenberg, *Cell Rep. Phys. Sci.*, 2025, **6**, 102653.

48 P. Caprioglio, S. Caicedo-Dávila, T. C.-J. Yang, C. M. Wolff, F. Peña-Camargo, P. Fiala, B. Rech, C. Ballif, D. Abou-Ras, M. Stolterfoht, S. Albrecht, Q. Jeangros and D. Neher, *ACS Energy Lett.*, 2021, **6**, 419–428.

49 W. Rehman, D. P. McMeekin, J. B. Patel, R. L. Milot, M. B. Johnston, H. J. Snaith and L. M. Herz, *Energy Environ. Sci.*, 2017, **10**, 361–369.

50 N. Aristidou, S. Pont, I. Sanchez-Molina, T. Chotchunangatchaval, S. Wheeler, J. R. Durrant and S. A. Haque, *Energy Environ. Sci.*, 2016, **9**, 1655–1660.

51 Y.-R. Wang, G. Yeong Kim, E. Kotomin, D. Moia and J. Maier, *JPhys Energy*, 2022, **4**, 011001.

52 Z. Xu, X. Zhong, T. Hu, J. Hu, A. Kahn and B. P. Rand, *J. Am. Chem. Soc.*, 2024, **146**, 33368–33377.

53 E. M. Hutter, J.-J. Hofman, M. L. Petrus, M. Moes, R. D. Abellon, P. Docampo and T. J. Savenije, *Adv. Energy Mater.*, 2017, **7**, 8.

54 B. Krogmeier, F. Staub, D. Grabowski, U. Rau and T. Kirchartz, *Sustainable Energy Fuels*, 2018, **2**, 1027–1034.

55 L. Kruckemeier, B. Krogmeier, Z. Liu, U. Rau and T. Kirchartz, *Adv. Energy Mater.*, 2021, **11**, 19.

56 I. Levine, A. Al-Ashouri, A. Musiienko, H. Hempel, A. Magomedov, A. Drevilkauskaite, V. Getautis, D. Menzel, K. Hinrichs, T. Unold, S. Albrecht and T. Dittrich, *Joule*, 2021, **5**, 2915–2933.

57 T. Kirchartz, J. A. Márquez, M. Stolterfoht and T. Unold, *Adv. Energy Mater.*, 2020, **10**, 1904134.

58 J. A. Nelson, *The Physics of Solar Cells*, World Scientific Publishing Company, 2003.

59 J. Thiesbrummel, S. Shah, E. Gutierrez-Partida, F. Zu, F. Peña-Camargo, S. Zeiske, J. Diekmann, F. Ye, K. P. Peters, K. O. Brinkmann, P. Caprioglio, A. Dasgupta, S. Seo, F. A. Adeleye, J. Warby, Q. Jeangros, F. Lang, S. Zhang, S. Albrecht, T. Riedl, A. Armin, D. Neher, N. Koch, Y. Wu, V. M. Le Corre, H. Snaith and M. Stolterfoht, *Nat. Energy*, 2024, **9**, 664–676.

60 R. Wang, X. Liu, S. Yan, N. Meng, X. Zhao, Y. Chen, H. Li, S. M. H. Qaid, S. Yang, M. Yuan and T. He, *Nat. Commun.*, 2024, **15**, 8899.

61 D. Pu, X. Zhang, H. Fang, W. Shen, G. Chen, W. Chen, P. Jia, G. Li, H. Guan, L. Huang, Y. Zhou, J. Wang, W. Zheng, W. Meng, G. Fang and W. Ke, *Sci. Adv.*, 2025, **11**, eady3621.

62 Z. Wu, Y. Zhao, C. Wang, T. Ma, C. Chen, Y. Liu, T. Jia, Y. Zhai, C. Chen, C. Zhang, G. Cao, Z. Yang, D. Zhao and X. Li, *Adv. Mater.*, 2025, **37**, 2412943.

63 Z. Yi, W. Wang, R. He, J. Zhu, W. Jiao, Y. Luo, Y. Xu, Y. Wang, Z. Zeng, K. Wei, J. Zhang, S.-W. Tsang, C. Chen, W. Tang and D. Zhao, *Energy Environ. Sci.*, 2024, **17**, 202–209.

64 L. Du, F. Cao, R. Meng, Y. Zhang, J. Zhang, Z. Gao, C. Chen, C. Li, D. Zhao, J. Ye, Z. Li and C. Xiao, *Nat. Commun.*, 2025, **16**, 8080.

65 J. Xu, C. C. Boyd, Z. J. Yu, A. F. Palmstrom, D. J. Witter, B. W. Larson, R. M. France, J. Werner, S. P. Harvey, E. J. Wolf, W. Weigand, S. Manzoor, M. F. A. M. van Hest, J. J. Berry, J. M. Luther, Z. C. Holman and M. D. McGehee, *Science*, 2020, **367**, 1097–1104.

66 J. Zhang, J. Duan, Q. Guo, Q. Zhang, Y. Zhao, H. Huang, Y. Duan and Q. Tang, *ACS Energy Lett.*, 2022, **7**, 3467–3475.

67 L. Yang, Z. Fang, Y. Jin, H. Feng, B. Deng, L. Zheng, P. Xu, J. Chen, X. Chen, Y. Zhou, C. Shi, W. Gao, J. Yang, X. Xu, C. Tian, L. Xie and Z. Wei, *Adv. Mater.*, 2024, **36**, 2311923.

68 A. J. Knight and L. M. Herz, *Energy Environ. Sci.*, 2020, **13**, 2024–2046.

69 K. A. Elmestekawy, A. D. Wright, K. B. Lohmann, J. Borchert, M. B. Johnston and L. M. Herz, *ACS Nano*, 2022, **16**, 9640–9650.